Effects of spatial coherence in diffraction phase microscopy

Chris Edwards,[1] Basanta Bhaduri,[2] Tan Nguyen,[2] Benjamin G. Griffin,[1] Hoa Pham,[2] Taewoo Kim,[2] Gabriel Popescu,[2] and Lynford L. Goddard[1,*]

[1]*Photonic Systems Laboratory, Department of Electrical and Computer Engineering, Micro and Nanotechnology Laboratory, University of Illinois at Urbana-Champaign, Urbana, Illinois 61801, USA*
[2]*Quantitative Light Imaging Laboratory, Department of Electrical and Computer Engineering, Beckman Institute for Advanced Science and Technology, University of Illinois at Urbana-Champaign, Urbana, Illinois 61801, USA*
[*]*lgoddard@illinois.edu*

Abstract: Quantitative phase imaging systems using white light illumination can exhibit lower noise figures than laser-based systems. However, they can also suffer from object-dependent artifacts, such as halos, which prevent accurate reconstruction of the surface topography. In this work, we show that white light diffraction phase microscopy using a standard halogen lamp can produce accurate height maps of even the most challenging structures provided that there is proper spatial filtering at: 1) the condenser to ensure adequate spatial coherence and 2) the output Fourier plane to produce a uniform reference beam. We explain that these object-dependent artifacts are a high-pass filtering phenomenon, establish design guidelines to reduce the artifacts, and then apply these guidelines to eliminate the halo effect. Since a spatially incoherent source requires significant spatial filtering, the irradiance is lower and proportionally longer exposure times are needed. To circumvent this tradeoff, we demonstrate that a supercontinuum laser, due to its high radiance, can provide accurate measurements with reduced exposure times, allowing for fast dynamic measurements.

© 2014 Optical Society of America

References and links

1. G. Popescu, *Quantitative Phase Imaging of Cells and Tissues*, McGraw-Hill biophotonics (McGraw-Hill, 2011).
2. G. Popescu, T. Ikeda, R. R. Dasari, and M. S. Feld, "Diffraction phase microscopy for quantifying cell structure and dynamics," Opt. Lett. **31**(6), 775–777 (2006).
3. C. Edwards, A. Arbabi, G. Popescu, and L. L. Goddard, "Optically monitoring and controlling nanoscale topography during semiconductor etching," Light Sci. Appl. **1**(9), e30 (2012).
4. C. Edwards, K. Wang, R. Zhou, B. Bhaduri, G. Popescu, and L. L. Goddard, "Digital projection photochemical etching defines gray-scale features," Opt. Express **21**(11), 13547–13554 (2013).
5. R. Zhou, G. Popescu, and L. L. Goddard, "22 nm node wafer inspection using diffraction phase microscopy and image post-processing," Proc. SPIE **8681**, 8610G (2013).
6. Y. Park, G. Popescu, K. Badizadegan, R. R. Dasari, and M. S. Feld, "Diffraction phase and fluorescence microscopy," Opt. Express **14**(18), 8263–8268 (2006).
7. N. Lue, W. Choi, K. Badizadegan, R. R. Dasari, M. S. Feld, and G. Popescu, "Confocal diffraction phase microscopy of live cells," Opt. Lett. **33**(18), 2074–2076 (2008).
8. Y. K. Park, M. Diez-Silva, G. Popescu, G. Lykotrafitis, W. Choi, M. S. Feld, and S. Suresh, "Refractive index maps and membrane dynamics of human red blood cells parasitized by Plasmodium falciparum," Proc. Natl. Acad. Sci. U.S.A. **105**(37), 13730–13735 (2008).
9. Y. Park, T. Yamauchi, W. Choi, R. Dasari, and M. S. Feld, "Spectroscopic phase microscopy for quantifying hemoglobin concentrations in intact red blood cells," Opt. Lett. **34**(23), 3668–3670 (2009).
10. Y. K. Park, C. A. Best, T. Auth, N. S. Gov, S. A. Safran, G. Popescu, S. Suresh, and M. S. Feld, "Metabolic remodeling of the human red blood cell membrane," Proc. Natl. Acad. Sci. U.S.A. **107**(4), 1289–1294 (2010).

11. Y. K. Park, C. A. Best, K. Badizadegan, R. R. Dasari, M. S. Feld, T. Kuriabova, M. L. Henle, A. J. Levine, and G. Popescu, "Measurement of red blood cell mechanics during morphological changes," Proc. Natl. Acad. Sci. U.S.A. **107**(15), 6731–6736 (2010).
12. J. W. Kang, N. Lue, C.-R. Kong, I. Barman, N. C. Dingari, S. J. Goldfless, J. C. Niles, R. R. Dasari, and M. S. Feld, "Combined confocal Raman and quantitative phase microscopy system for biomedical diagnosis," Biomed. Opt. Express **2**(9), 2484–2492 (2011).
13. S. Witte, A. Plauşka, M. C. Ridder, L. van Berge, H. D. Mansvelder, and M. L. Groot, "Short-coherence off-axis holographic phase microscopy of live cell dynamics," Biomed. Opt. Express **3**(9), 2184–2189 (2012).
14. B. Bhaduri, H. Pham, M. Mir, and G. Popescu, "Diffraction phase microscopy with white light," Opt. Lett. **37**(6), 1094–1096 (2012).
15. H. Pham, B. Bhaduri, H. Ding, and G. Popescu, "Spectroscopic diffraction phase microscopy," Opt. Lett. **37**(16), 3438–3440 (2012).
16. P. Girshovitz and N. T. Shaked, "Compact and portable low-coherence interferometer with off-axis geometry for quantitative phase microscopy and nanoscopy," Opt. Express **21**(5), 5701–5714 (2013).
17. H. V. Pham, B. Bhaduri, K. Tangella, C. Best-Popescu, and G. Popescu, "Real time blood testing using quantitative phase imaging," PLoS ONE **8**(2), e55676 (2013).
18. T. Slabý, P. Kolman, Z. Dostál, M. Antoš, M. Lošťák, and R. Chmelík, "Off-axis setup taking full advantage of incoherent illumination in coherence-controlled holographic microscope," Opt. Express **21**(12), 14747–14762 (2013).
19. J. W. Goodman, "Statistical properties of laser speckle patterns," in *Laser Speckle and Related Phenomena* (Springer, 1975).
20. P. Gao, B. Yao, I. Harder, N. Lindlein, and F. J. Torcal-Milla, "Phase-shifting Zernike phase contrast microscopy for quantitative phase measurement," Opt. Lett. **36**(21), 4305–4307 (2011).
21. T. Wilson and C. J. R. Sheppard, "The halo effect of image processing by spatial frequency filtering," Optik (Stuttg.) **59**(1), 19–23 (1981).
22. H. V. Pham, C. Edwards, L. L. Goddard, and G. Popescu, "Fast phase reconstruction in white light diffraction phase microscopy," Appl. Opt. **52**(1), A97–A101 (2013).
23. J. W. Goodman, *Introduction to Fourier Optics* (Roberts & Company, 2005).
24. B. E. A. Saleh and M. C. Teich, *Fundamentals of Photonics* (Wiley, 2013).
25. M. Born and E. Wolf, *Principles of optics,* 7th (expanded) ed. (Pergamon Press, 1999).
26. T. Nguyen, C. Edwards, L. Goddard, and G. Popescu, "Quantitative phase imaging with partially coherent illumination," (to be submitted).
27. T. Kim, R. Zhu, T. H. Nguyen, R. Zhou, C. Edwards, L. L. Goddard, and G. Popescu, "Deterministic signal associated with a random field," Opt. Express **21**(18), 20806–20820 (2013).
28. B. Bhaduri, D. Wickland, R. Wang, V. Chan, R. Bashir, and G. Popescu, "Cardiomyocyte Imaging Using Real-Time Spatial Light Interference Microscopy (SLIM)," PLoS ONE **8**(2), e56930 (2013).
29. B. Bhaduri, K. Tangella, and G. Popescu, "Fourier phase microscopy with white light," Biomed. Opt. Express **4**(8), 1434–1441 (2013).
30. T. H. Nguyen and G. Popescu, "Spatial Light Interference Microscopy (SLIM) using twisted-nematic liquid-crystal modulation," Biomed. Opt. Express **4**(9), 1571–1583 (2013).
31. Z. Wang, L. Millet, M. Mir, H. Ding, S. Unarunotai, J. Rogers, M. U. Gillette, and G. Popescu, "Spatial light interference microscopy (SLIM)," Opt. Express **19**(2), 1016–1026 (2011).
32. M. Mir, K. Tangella, and G. Popescu, "Blood testing at the single cell level using quantitative phase and amplitude microscopy," Biomed. Opt. Express **2**(12), 3259–3266 (2011).
33. J. Gass, A. Dakoff, and M. K. Kim, "Phase imaging without 2pi ambiguity by multiwavelength digital holography," Opt. Lett. **28**(13), 1141–1143 (2003).
34. C. J. Mann, P. R. Bingham, V. C. Paquit, and K. W. Tobin, "Quantitative phase imaging by three-wavelength digital holography," Opt. Express **16**(13), 9753–9764 (2008).
35. M. T. Rinehart, N. T. Shaked, N. J. Jenness, R. L. Clark, and A. Wax, "Simultaneous two-wavelength transmission quantitative phase microscopy with a color camera," Opt. Lett. **35**(15), 2612–2614 (2010).

1. Introduction

1.1. Quantitative phase imaging (QPI)

QPI methods exploit the fact that the phase of the imaging field is typically much more informative than its amplitude [1]. The relative phase shifts measured using these techniques contain topographical as well as refractive index information about the specimen under investigation. Diffraction phase microscopy (DPM) is a QPI method that was first demonstrated in 2006 using laser illumination [2]. DPM utilizes a compact Mach-Zehnder interferometer to combine many of the best attributes of current QPI methods [2–4]. This common-path geometry inherently cancels out most mechanisms responsible for noise and the single-shot measurement allows acquisition rates limited only by the speed of the camera

employed. This technique does not require coating or staining of the specimen and is therefore non-destructive. This unique collection of features enables the DPM system to accurately monitor the dynamics of various nanoscale phenomena in their natural environments. Our laser DPM system operates in both transmission and reflection in order to accommodate both transparent and reflective samples and is currently being used to monitor wet etching [3], photochemical etching [4], surface wetting and evaporation, expansion and deformation of materials, and to perform semiconductor wafer defect detection [5]. Other research groups have exploited the multimodal imaging capabilities of DPM by combining it with other imaging modalities such as fluorescence and confocal/Raman in order to study morphology and dynamics of biological structures [6–13].

Recently, white light DPM (wDPM) was developed for use in biological applications [9, 14–17]. White light imaging systems using standard halogen lamp illumination can exhibit lower spatial phase noise than their laser counterparts [3, 4, 14, 18]. This is a result of the lower coherence, both spatially and temporally, which reduces some noise mechanisms such as speckle [19]. Unfortunately, white light systems can also exhibit some object-dependent artifacts not present in laser systems. In this work, we show that both a lack of spatial coherence and inadequate spatial filtering of the reference beam can individually cause high-pass filtering of the DPM image, resulting in the halo effect and shade-off. The halo effect can result in erroneous height values, typically negative, around the perimeter of an object. Shade-off occurs in conjunction with the halo effect and results in the center of large area objects having reduced contrast in measured intensity and/or reduced phase shifts in QPI [20, 21]. By conducting a thorough theoretical and experimental investigation, we present guidelines for obtaining adequate spatial coherence and filtering and demonstrate the removal of these object-dependent artifacts.

The spatial filtering used to obtain adequate spatial coherence reduces the illuminating power. This in turn increases the necessary camera exposure time and prevents high-throughput real-time imaging [17]. We solve this tradeoff by showing that the much higher radiance of a supercontinuum laser results in accurate measurements with low exposure times.

1.2 Experimental setup

Figure 1 shows a schematic of the wDPM system, which can be placed at the output port of a conventional light microscope. We create an interferometer by using a diffraction grating, a 4f lens system, and a spatial light modulator (SLM). The diffraction grating creates multiple copies of the image at various angles, some of which are captured by the 1st lens. Under a 4f configuration, the first lens takes the Fourier transform. An SLM is placed in the Fourier plane where the spatial filtering is performed. Here, all of the orders except the 0 and + 1 are blocked. The 1st order contains the full image and the 0th order is filtered down using a small circular mask which serves as a pinhole. The pinhole diameter is chosen to be small enough such that, after the 2nd lens takes another Fourier transform, the field approaches a plane wave and is uniform across the CCD to serve as our reference beam. The two beams interfere at the CCD to produce an interferogram. This interferogram is a spatially modulated signal, which allows us to extract the phase information via a Hilbert transform [3, 22].
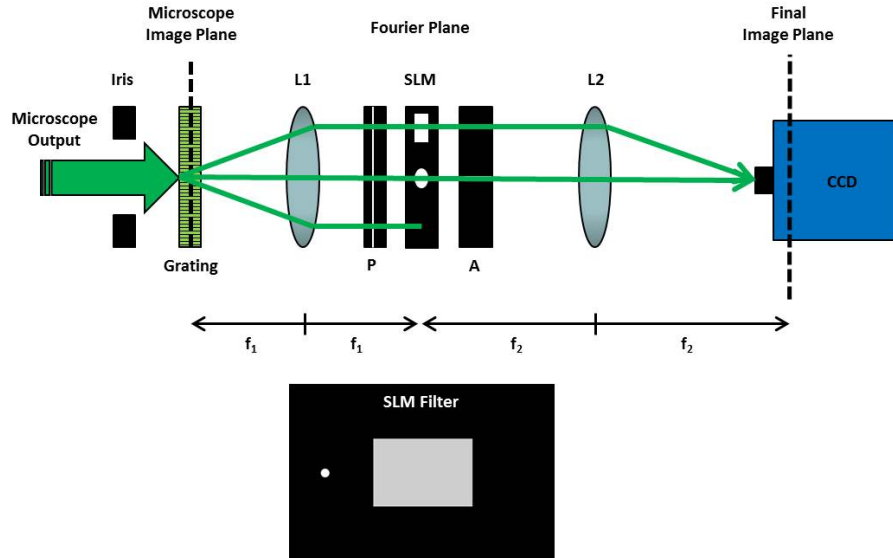
Fig. 1. wDPM imaging system. A diffraction grating, 4f lens system, and a spatial light modulator (SLM) are used to achieve interference. The SLM performs spatial filtering and one order can be gray-scaled in order to match intensities and optimize the fringe visibility. The interferogram captured by the CCD is a spatially modulated signal, which allows us to extract the phase information via a Hilbert transform and reconstruct the surface topography.

1.3 Spatial coherence in conventional microscopes

Commercial microscopes are often incorporated into experimental setups when researching and developing new imaging techniques. Unfortunately, most microscopes are not designed for quantitative phase imaging. For example, the condenser aperture of the Zeiss Z2 Axio-Imager only closes down to a numerical aperture (NA_{con}) of about 0.09. This results in a coherence area much smaller than the field-of-view (FOV) for typical objectives. Note that for laser-based systems, this is not an issue since the effective NA_{con} is approximately zero. The normalized mutual intensity function formed by the circular aperture of the condenser (actually a heptagon shaped iris) under partially coherent illumination is [23, 24],

$$\left| g(x_1, x_2, y_1, y_2) \right| = \left| \frac{2J_1(\pi\rho\theta_s / \lambda)}{\pi\rho\theta_s / \lambda} \right| \qquad (1)$$

where J_1 is a Bessel function of the first kind, $\rho = \sqrt{(x_2 - x_1)^2 + (y_2 - y_1)^2}$, $\theta_s = 2NA_{con}$ is the angle subtended by the source, and λ is the mean wavelength of the illumination. The spatial coherence radius, ρ_c, is often defined as the distance from the peak to its first zero (radius of coherence area) [24, 25]. Thus, $\rho_c = 0.61\lambda / NA_{con}$. For our case, with a mean wavelength of 574 nm and an $NA_{con} = 0.09$, we obtain $\rho_c = 3.9$ μm. Throughout this paper, images are captured using a 20X, 0.8 NA objective resulting in a lateral resolution of 0.87 μm and a FOV of 135 x 180 μm^2 in the sample plane. Thus, the radius of a circle that circumscribes the FOV is r = 112 μm. Intuitively, it is desirable to have $\rho_c \geq$ r. As we will later show, this condition is actually too weak and it is necessary to have the mutual intensity function be nearly flat over the object being measured, which as a general rule of thumb, requires that the coherence diameter be at least ten times the lateral extent of the object.

To experimentally determine ρ_c, the grating was removed from the wDPM setup and the Fourier plane was imaged to measure the angular spread of the source. By taking the inverse Fourier transform, we obtain the autocorrelation function via the Wiener-Khintchine theorem

[1, 23, 24]. Figures 2(a) and 2(b) show a 2-dimensional (2D) image of the Fourier plane and the corresponding 1-dimensional (1D) k_x slice. The maximum transverse component of the wave vector ($k_\rho = \sqrt{k_x^2 + k_y^2} = k_0 NA_{con}$) is inversely proportional to the degree of spatial coherence. As the condenser aperture approaches zero, full spatial coherence across the FOV is achieved. Figures 2(c) and 2(d) show the resulting normalized 2D autocorrelation function and 1D slice. The peak to first zero distance is measured to be $\rho_c = 4.0$ μm. The coherence area is simply $A_c = \pi\rho_c^2$ [24]. The spatial coherence present in this conventional microscope, even with the condenser completely closed is not adequate for proper quantitative phase imaging of many structures.
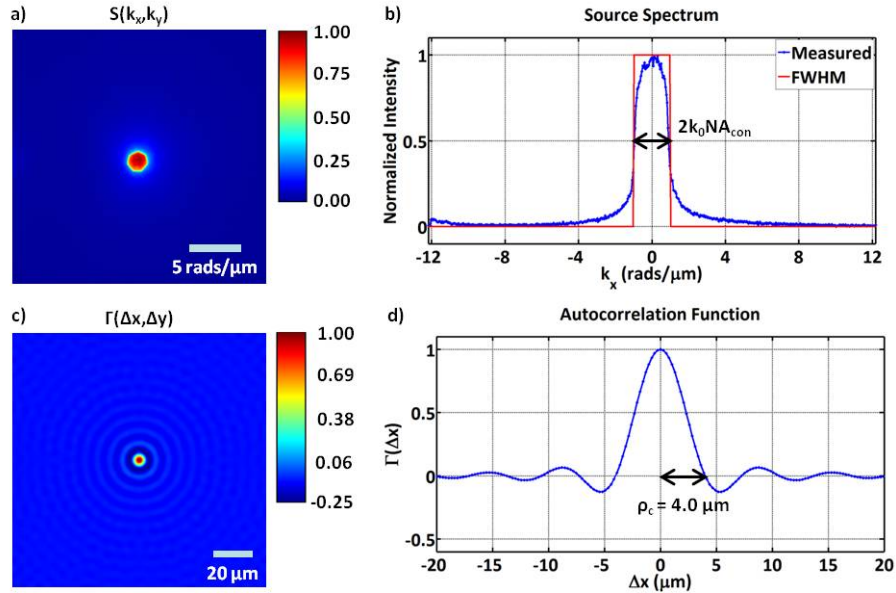

Fig. 2. Spatial coherence of the wDPM imaging system. (a) Angular spectrum of the source showing the full-width at half-maximum (FWHM) approximation. (b) Horizontal slice taken through the origin in (a). The radius of the unscattered light circle is approximately $k_0 NA_{con}$. (c) Autocorrelation function computed from (a). (d) Horizontal slice taken through origin in (c). The spatial coherence radius is $\rho_c = 4.0$ μm.

In addition to spatial coherence, wDPM also needs adequate temporal coherence to produce proper interferograms. In the Appendix, we present measurement data showing that the temporal coherence of the wDPM light source is at least an order of magnitude larger than what is needed to measure the samples discussed in this paper.

2. Theoretical analysis

2.1 DPM with partially coherent illumination

In this section, we present a theoretical analysis of the phase measured by DPM under partially coherent illumination. The full derivation will be presented in [26]. To simplify the analysis, low-pass filtering from the microscope's objective lens is ignored. This phenomenon is already well understood and moreover, it is negligible when imaging large objects with high NA objectives. Let U_1 be the imaging field and U_0 be the reference field. Both of these are random fields, but the CCD measures mutual intensity functions, which are deterministic [27]. The interferogram captured by the CCD can be written as:

$$I(\mathbf{r}) = \left\langle \left| U_0(\mathbf{r},t) + U_1(\mathbf{r},t) \right|^2 \right\rangle_T = I_0(\mathbf{r}) + I_1(\mathbf{r}) + 2\Re\left\{ \left\langle U_0^*(\mathbf{r},t) U_1(\mathbf{r},t) \right\rangle_T \right\} \qquad (2)$$

where I_0 and I_1 are the intensities of the reference and imaging fields respectively. The modulation term contains the temporal cross-correlation of the two interfering fields. In DPM, we recover the phase image from the modulation term as [26]:

$$\phi(\mathbf{r}) = \arg\left[T(\mathbf{r})\right] - \arg\left[\left(\Gamma_{illum}^*(\mathbf{r})\tilde{\Pi}_{slm}(\mathbf{r})\right) \otimes T(\mathbf{r})\right] \tag{3}$$

where T is the complex-valued transmittance function of the sample, Π_{slm} is the SLM filter aperture function, a tilde denotes a Fourier transform, $\otimes$ is the 2D convolution operator, $\Gamma_{illum}(\mathbf{r}-\mathbf{r}') \equiv \left\langle U_{illum}(\mathbf{r},t)U_{illum}^*(\mathbf{r}',t)\right\rangle_T$ is the mutual intensity function, $U_{illum} \equiv \tilde{U}_s(\mathbf{r},t) \otimes \tilde{\Pi}_{con}(\mathbf{r})$ is the illumination field that interacts with the sample, $\tilde{U}_s$ is the field emitted by the halogen source (in a conjugate Fourier plane), and Π_{con} is the condenser aperture function. Note that Γ_{illum} that depends only on $\mathbf{r}-\mathbf{r}'$ since we assume the source field $\tilde{U}_s$ is shift invariant or isoplanatic [24, 27].

The 1st term in (4), $\phi_1(\mathbf{r}) = \arg\left[T(\mathbf{r})\right]$ is the phase information from the sample and is referred to as the true phase image. The 2nd term $\phi_0(\mathbf{r}) = \arg\left[\left(\Gamma_i^*(\mathbf{r})\tilde{\Pi}_{slm}(\mathbf{r})\right) \otimes T(\mathbf{r})\right]$ is a low-pass filtered (LPF) version of the true phase image and is referred to as the cancellation phase. Thus, the relative phase measured by DPM is the true phase image minus a LPF version of itself. This subtraction produces a high pass filtered (HPF) image, which makes the lower spatial frequencies of the sample unattainable. To recover the true phase image, the 2nd term needs to be spatially constant, which requires that $\Gamma_{illum}^*(\mathbf{r})\tilde{\Pi}_{slm}(\mathbf{r})$ be uniform across the FOV. This requires that: (1) the condenser aperture be closed down far enough to ensure adequate spatial coherence and (2) the SLM filter be small enough to ensure a uniform reference beam.

2.2 The effects of spatial filtering on DPM image formation

Figure 3 contains simulation results showing the effects of spatial filtering. The computed height is proportional to the measured phase [3]. Note that as the spatial filtering is improved, h_0 becomes flat and Δh approaches h_1. Figure 3 shows simulations of the true height image $h_1(\mathbf{r}) = \frac{\lambda}{2\pi\Delta n}\phi_1(\mathbf{r})$, the height of the cancellation field $h_0(\mathbf{r}) = \frac{\lambda}{2\pi\Delta n}\phi_0(\mathbf{r})$, the resulting height map, and the cross-section for polystyrene microbeads in immersion oil (Figs. 3(a-d)) and for red blood cells (RBCs) in Coulter solution (Figs. 3(e-h)) under non-ideal conditions. The halo can be seen in Fig. 3(d) and the halo and negative dimple can be seen in Fig. 3(h). The halo and shade-off are both produced simultaneously via the HPF effect. Such halos have been observed notoriously in phase contrast microscopy, as well as in high-throughput white light QPI systems [15, 17, 21, 28–31].
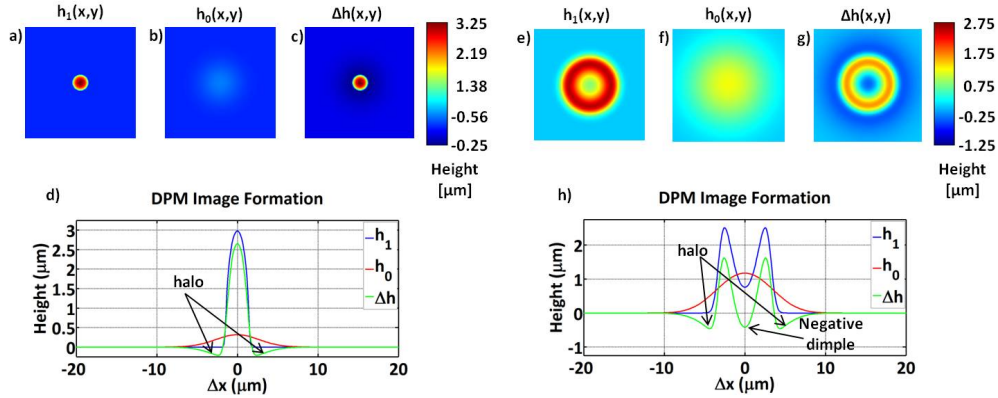
Fig. 3. DPM image formation. (a) Simulation of the ideal height map for a 3 μm diameter polystyrene microbead in immersion oil. (b) Simulated height from the cancellation field under non-ideal conditions. (c) Simulation of recovered height, which is the difference between (a) and (b). (d) Horizontal slice taken through origin showing (a-c). Note that cancellation field in (b) contains residues of the structure which results in the observed halo effect and a reduction in the measured height. (e-h) Corresponding simulations for a red blood cell in Coulter solution showing a reduction in the measured height as well as a halo and a negative dimple.

3. Experimental results

3.1 Spatial filtering study

Experiments were done to validate the theory presented above for DPM image formation. A quartz wafer was patterned and etched, resulting in a variety of 123 nm tall (as verified by the Alpha Step IQ Profilometer) square pillars with different lateral sizes, to serve as the calibration sample. Two key parameters: the NA of the condenser (NA_{con}) and the diameter of the SLM pinhole filter (D) were varied and DPM height images were collected. Figure 4(a) shows a plot of the investigated parameter space. The labels in Fig. 4(a) correspond to the operating points for subsequent subfigures.

Figure 4(b) shows the 0th order reference amplitude image (obtained by blocking the 1st order beam), the recovered height map, and corresponding cross-section under our previous wDPM operating conditions, e.g. with the condenser aperture closed ($NA_{con} = 0.09$) and the SLM pinhole diameter set to its optimum value (D = 355 μm). The optimum pinhole diameter is selected by first matching the circular filter of the SLM so that it inscribes the heptagon from the condenser aperture. This matched condition is represented by the solid line in Fig. 4(a). Height maps are obtained as the SLM pinhole size is reduced until the pillar height converges to its maximum value. Note that the heights converge as the diffraction pattern from the SLM pinhole, $\tilde{\Pi}_{slm}(\mathbf{r})$, becomes nearly uniform over the width of the central lobe of the mutual intensity function, $\Gamma_{illum}(\mathbf{r})$. Once this occurs, decreasing the SLM pinhole size further only increases noise and reduces fringe visibility. The SLM pinhole filter size is set at its optimum value for cases b, d, f and k. If the SLM pinhole size is larger than the matched condition, then scattered light containing important structural information about the sample will be removed from the final image. It corresponds to the region above the solid line in Fig. 4(a) where no data points reside.
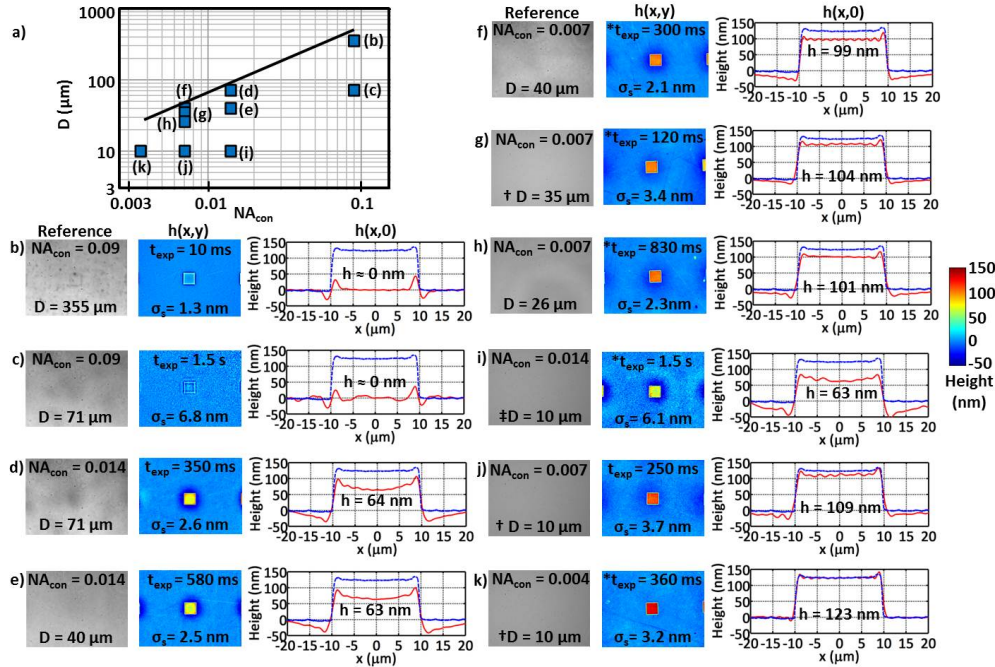
a)

1000

100

D (μm)

10

3
0.003   0.01   0.1
NA_con

(b)
(f) (d)
(h) (g) (e)
(k) (j) (i)

Reference   h(x,y)   h(x,0)
f) NA_con = 0.007   *t_exp = 300 ms   h = 99 nm
   D = 40 μm   σ_s = 2.1 nm

g) NA_con = 0.007   *t_exp = 120 ms   h = 104 nm
   † D = 35 μm   σ_s = 3.4 nm

Reference   h(x,y)   h(x,0)
b) NA_con = 0.09   t_exp = 10 ms   h ≈ 0 nm
   D = 355 μm   σ_s = 1.3 nm

h) NA_con = 0.007   *t_exp = 830 ms   h = 101 nm
   D = 26 μm   σ_s = 2.3 nm

c) NA_con = 0.09   t_exp = 1.5 s   h ≈ 0 nm
   D = 71 μm   σ_s = 6.8 nm

i) NA_con = 0.014   *t_exp = 1.5 s   h = 63 nm
   ‡D = 10 μm   σ_s = 6.1 nm

150
100
50
0
-50
Height (nm)

d) NA_con = 0.014   t_exp = 350 ms   h = 64 nm
   D = 71 μm   σ_s = 2.6 nm

j) NA_con = 0.007   t_exp = 250 ms   h = 109 nm
   † D = 10 μm   σ_s = 3.7 nm

e) NA_con = 0.014   t_exp = 580 ms   h = 63 nm
   D = 40 μm   σ_s = 2.5 nm

k) NA_con = 0.004   *t_exp = 360 ms   h = 123 nm
   †D = 10 μm   σ_s = 3.2 nm

Fig. 4. The effects of spatial filtering in DPM. (a) Log-log plot showing the investigated parameter space of SLM pinhole filter diameter (D) and condenser numerical aperture (NA_con). The solid line represents the matched filter condition. Labels b-k correspond to the operating point for subsequent subfigures. (b-k) 0th order reference amplitude images, recovered height images, and corresponding height cross-sections. The cross-section figures show the wDPM profile in red and the Alpha Step profile in blue. The spatial noise (σ_s) and exposure times (t_exp) are also listed for each subfigure. Both adequate spatial coherence and proper spatial filtering are required in order to properly reconstruct the height maps using wDPM. As both the condenser NA and the SLM pinhole diameter are reduced, aberrations such as halo and shade-off are reduced and the pillar heights converge to their proper value (h = 123 nm) as verified with the Alpha Step IQ Profilometer. † denotes a physical pinhole in the SLM plane, and ‡ denotes a physical pinhole with SLM attenuation to better match intensities. * indicates a gain setting of 2 on the Zeiss AxioCam MRm CCD.

In Fig. 4(b), the recovered phase only contains information about the edges of the pillar and the height in the center of the pillar is the same as the background. Thus, the measured height is approximately zero. Note that the reference is not filtered strongly enough, and as a result, it is not uniform. Residuals of the pillar can clearly be seen. The exposure time was set at t_{exp} = 10 ms for this acquisition. In subsequent figures, auto-exposure was used to select t_{exp} due to the varying levels of light at the CCD. In Fig. 4(c), with NA_{con} = 0.09, the SLM pinhole diameter was set to 71 μm, which is the optimum condition for the next lowest NA_{con} value (i.e. Figure 4(d)). Comparing Figs. 4(b) and 4(c), we see that reducing the SLM pinhole diameter beyond its optimum value for a given NA_{con} does not improve the quantitative nature of the recovered phase, but only decreases the amount of light that makes it to the CCD, thereby increasing the required exposure time and raising the noise floor. We were not able to capture images for NA_{con} = 0.09 with SLM pinhole diameters smaller than 71 μm due to a poor signal-to-noise ratio (SNR).

To further reduce the numerical aperture of the condenser beyond the conventional limit (NA_{con} = 0.09), a small 400 μm pinhole (NA_{con} = 0.014) was placed inside the condenser turret and the system was realigned. This increases the coherence radius from ρ_c = 3.9 μm to ρ_c = 25 μm. Figure 4(d) shows the 0th order reference amplitude image along with its recovered height map. Here, the SLM pinhole is the same size as in Fig. 4(c), but NA_{con} is about six times smaller. Despite the reference still containing small residues of the pillar and

not being perfectly uniform, the height map recovered under these conditions is beginning to show the structure of the pillar. Figure 4(e) shows a factor of two reduction in the SLM pinhole diameter for the same NA_{con} = 0.014 value. As predicted by Eq. (4), there is no discernible change in the height map when the SLM pinhole is reduced beyond its optimum value; however, a reduction in the pinhole diameter requires the exposure time to increase. Again, this is because once the pinhole is small enough, its diffraction pattern becomes uniform over the mutual intensity function's central lobe, which now becomes dominant, and further decrease in the pinhole diameter has no effect. To further reduce the numerical aperture of the condenser, a 200 μm pinhole was placed into the condenser turret (NA_{con} = 0.0072, ρ_c = 50 μm). The optimum SLM pinhole diameter for NA_{con} = 0.0072 is D = 40 μm. Under these conditions, the halo in Fig. 4(f) is slightly reduced and the measured height (h = 99 nm) is closer to the Profilometer value (h = 123 nm). The gain on the CCD was set to 2, which lowered the required exposure time from about 600 ms down to 300 ms.

Figures 4(g) and 4(h) show a comparison between a 35 μm physical pinhole and a 2x2 pixel (26 μm) SLM filter with NA_{con} = 0.0072. This comparison was done to test whether the measured 400:1 contrast ratio of the SLM or the fact that a 2x2 pixel filter is square and not circular has a considerable effect on the recovered height map. These effects appear to be negligible. It is important though to note that the exposure time was higher for the SLM filter than the physical pinhole due to the presence of the crossed polarizers required with the SLM, which decreases the power in the interferogram by at least a factor of two.

Figures 4(i)-4(k) compare different NA_{con} values with a 10 μm physical pinhole. This is the typical pinhole diameter used in laser DPM because it produces an adequately uniform reference across the CCD for laser DPM [3, 4]. Figure 4(i) required additional attenuation from the SLM to get adequate fringe visibility, but the SLM cut the power by at least 2x, resulting in a large exposure time, t_{exp} = 1.5 s, and additional noise in the final image. Figure 4(j) looks nearly identical to 4(f), 4(g), and 4(h) showing that reducing the SLM pinhole size below the optimum value does not bring back the low frequency content to the image. Figure 4(k) shows that using a 100 μm pinhole in the condenser (NA_{con} = 0.0036, ρ_c = 100 μm) along with a 10 μm pinhole in the SLM plane allows for proper reconstruction of the 20 μm wide pillar. The minimum exposure time under proper imaging conditions was 360 ms. The exposure time increases with decreasing NA_{con}, decreasing D, or using an SLM that requires polarizers. It is also important to note that the exposure time can be set arbitrarily low by increasing the CCD's gain factor, but at the expense of lower SNR since noise is amplified along with signal. Ideally, a brighter source should be used for fast, accurate, low-noise imaging.

This spatial filtering study shows the importance of maintaining proper spatial coherence and filtering in DPM.

3.2 Required spatial coherence for a given object size

Figure 5 contains cross-sections of square pillars of different widths taken with various NA_{con} using the optimum SLM pinhole filter size for each case. This study indicates that larger lateral features are more difficult to quantitatively reconstruct and require a larger degree of spatial coherence. This is due to the simple fact that larger features in the spatial domain map more information to lower frequencies in the spatial frequency domain. The low frequency information is lost by the HPF effects in DPM if proper filtering is not obtained. For NA_{con} = 0.09, 0.014, 0.0072, and 0.0036, the corresponding spatial coherence diameters are $2\rho_c$ = 7.8, 50, 100, and 200 μm, respectively.
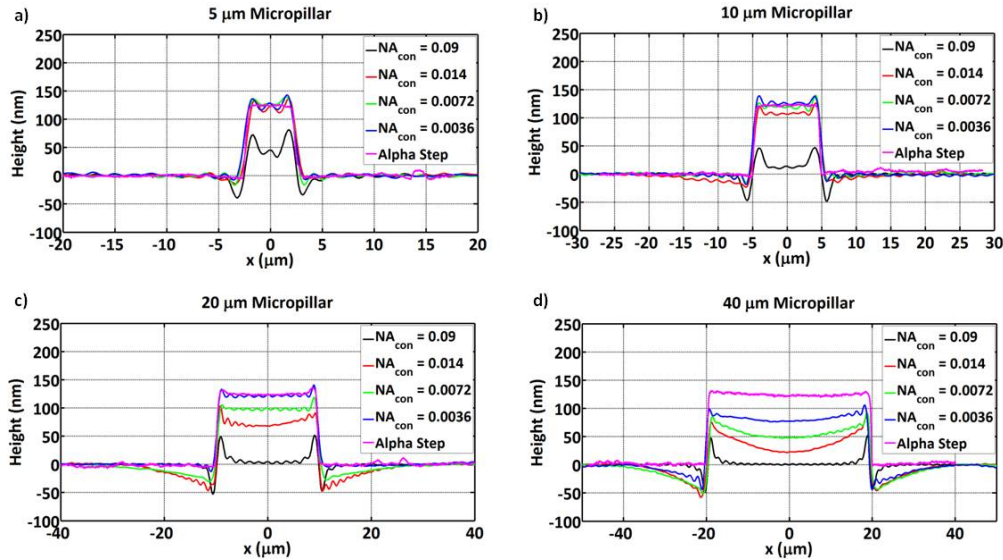
Fig. 5. Required spatial coherence for a given object size. Cross-sections were taken of square micropillars of different widths for various condenser numerical apertures using the optimum SLM pinhole filter size for each case. (a-d) 5, 10, 20, and 40 μm wide square pillars respectively. As the condenser NA is reduced and the SLM filter is optimized, the recovered structure becomes more quantitatively correct. Halo and shade-off disappear simultaneously as the pillar height converges to the proper value. Larger objects require more spatial coherence (smaller NA_{con}) to image properly. The 5, 10, and 20 μm wide pillars image properly for $NA_{con} \leq 0.014$, 0.0072, and 0.0036, respectively. The 40 μm wide pillar will require an even smaller NA_{con} to image properly.

Figure 5(a) shows cross-sections of a 5 μm wide square pillar with varying NA_{con} values. A conventional microscope with the condenser fully closed ($NA_{con} = 0.09$) is not able to properly reproduce the height map even for a 5 μm wide square. The heights converge for all values of $NA_{con} \leq 0.014$. Note that the shape of the pillar is slightly distorted due to LPF effects from the objective (20X, $NA_{obj} = 0.8$) which broadens the edges due to convolution with the point spread function (PSF) and also causes a peak at the edges (Gibbs' phenomenon) due to missing high frequency components required to reconstruct the vertical edge. These effects are less apparent for larger structures, where the dimensions are much larger than the diffraction spot, which has a 0.87 μm radius in the sample plane. The dimensions of the squares were verified using the Alpha Step IQ Profilometer.

Figure 5(b) shows cross-sections of a 10 μm wide square pillar. All heights converge to the proper value for $NA_{con} \leq 0.0072$. Note that the height map produced with $NA_{con} = 0.014$ contains a small halo and reduction in height which is indicative of a lack of spatial coherence. For $NA_{con} = 0.09$, only the pillar's edges are visible and the center height of the pillar is nearly zero. Figure 5(c) shows similar cross-sections for a 20 μm wide pillar, which are the cross sections of the images presented in Fig. 6. The height converges to the proper value for $NA_{con} \leq 0.0036$. Figure 5(d) shows cross-sections for a 40 μm wide square pillar. Here, even with a 100 μm pinhole in the condenser ($NA_{con} = 0.0036$, $\rho_c = 100$ μm), the height of the pillar has not converged and aberrations are still present. This study shows that for a given size structure, the condenser NA must be chosen such that the coherence area is much greater than the FOV. The condition that the coherence area circle at least circumscribes the FOV is too weak; it is actually necessary that the mutual intensity function be relatively flat over the object of interest. For a 20X objective in our setup, the radius of a circle circumscribing the rectangular FOV is 112 μm. The spatial coherence radius with an $NA_{con} = 0.0036$ is $\rho_c = 100$ μm, yet we can only properly image structures that are 20 μm in diameter

or smaller. From this object size scaling study, we obtain a general rule of thumb that the coherence diameter, $2\rho_c$, should be at least ten times the lateral size of the object being measured.

A reduction in the halo can be seen for the various pillars as the condenser NA is reduced and the heights begin to converge. Actually, according to the model presented earlier, as the pinhole sizes are decreased, the depth of the halo will decrease but its width will increase until the halo blends into the background. This will occur simultaneously as the height converges to the proper value. Most biological specimens are smaller than 20 μm in diameter. Since we can properly reconstruct the height map of a flat pillar with abrupt edges, which is a more difficult case under Fourier analysis considerations due to the very broad spectrum of spatial frequency components, we should be able to correctly reconstruct height maps for many biological samples with minimal aberrations as we will show in the next section.

3.3 Halo reduction in microbeads and red blood cells

Figures 6(a)-6(c) show wDPM images of 3 μm polystyrene microbeads in immersion oil with an NA_{con} = 0.09, 0.036, and 0.0036, using a closed condenser, a 1 mm condenser iris, and a 100 μm condenser pinhole, respectively. Figure 6(d) shows an overlay of the corresponding cross-sections which were taken diagonally through the centers of both beads. With the condenser aperture closed (NA_{con} = 0.09), the measured heights of the beads are lower than their expected value. Care must be taken when imaging microbeads, especially with a lack of spatial coherence, since the measured heights are very sensitive to the focus. Defocusing the bead can actually result in a measured height much larger than the correct value. To avoid such issues, the most in-focus image was taken from a stack of 60 images with 200 nm z-sections. The cross-sections in Fig. 6(d) show a reduction in the halo and convergence to the correct height upon reducing the numerical aperture of the condenser. For 3 μm diameter beads, the calculated NA_{con} using our rule of thumb to achieve adequate spatial coherence is 0.024, which is in between our 1 mm iris and 400 μm pinhole. The 1 mm iris results in an NA_{con} = 0.036, which is enough to get the heights to converge, but a small halo remains. A 100 μm pinhole with an NA_{con} = 0.0036 was therefore used in an attempt to completely remove the halo. Here, the halo is removed and only a small amount of ringing remains, which is a result of the Gibbs' phenomenon mentioned earlier.
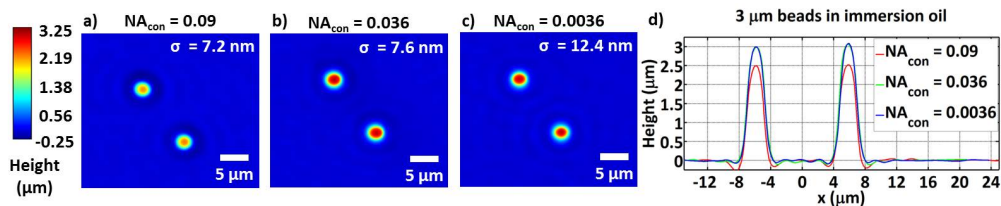

Fig. 6. Halo reduction in 3 μm diameter polystyrene microbeads in immersion oil. wDPM height map of microbeads for (a) closed condenser (NA_{con} = 0.09), (b) a 1mm iris placed in the condenser (NA_{con} = 0.036), and (c) a 100 μm pinhole placed in the condenser (NA_{con} = 0.0036). (d) Overlay showing cross-sections of a diagonal slice taken through the center of both beads. Closing the condenser beyond the conventional limit of NA_{con} = 0.09 to NA_{con} = 0.036 allows the heights to converge to their proper values, while additional spatial coherence using NA_{con} = 0.0036 is needed to remove the halo. Residual ringing is due to the Gibbs' phenomenon.

To observe how enhancing the spatial coherence and performing proper DPM filtering can improve the halo and shade-off in real-life applications, we imaged live red blood cells in Coulter solution. Figure 7(a) shows a wDPM height map taken with the 20X, 0.8 NA objective, NA_{con} = 0.09, and an exposure time of 20 ms. Figures 7(b) and 7(c) contain a cropped image of the RBC indicated by the dotted rectangle in (a) and the corresponding cross-section indicated by the dotted line in (b). However, the halo and negative dimple are clearly visible. Figures 7(d) and 7(e) show similar images captured using a 100 μm condenser

pinhole (NA_{con} = 0.0036). Figure 7(f) shows the cross-section of the RBC taken along the dotted line in (e). Figures 7(d)-7(f) show a drastic reduction in the halo, at the expense of larger exposure times. For real-time applications, long exposure times are impractical. In the next section, we show that a supercontinuum laser provides a good compromise between throughput and accuracy.
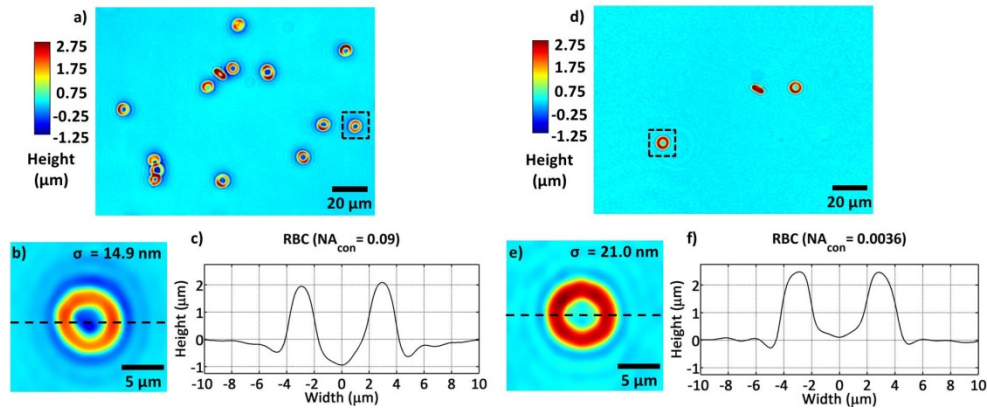

Fig. 7. Halo reduction in red blood cells (RBCs). (a) wDPM height map of live RBCs in Coulter solution with a closed condenser (NA_{con} = 0.09). (b) Cropped image showing a single RBC from (a). (c) Horizontal slice of the RBC in (b) showing the halo and negative dimple. (d-f) Corresponding images for a 100 μm pinhole placed in the condenser (NA_{con} = 0.0036) show a reduction in the halo and the removal of the negative dimple. Note that a small halo remains, which is attributed to the Gibbs' phenomenon.

3.4 DPM using a supercontinuum laser source

To get enough spatial coherence to measure an object that extends across most of the FOV for the widest FOV scenario (5X objective), the required NA is estimated to be 1.5×10^{-4}, which is 600x smaller than what is achievable with commercial microscopes. This would require a miniscule pinhole (~4 μm) to be placed in the condenser turret, which would result in a signal that is exceedingly weak, thereby requiring long exposure times. The long integration time makes this approach impractical given camera noise considerations and the inability to observe fast dynamics. As a practical compromise in a DPM system with a conventional incoherent source, measurements can be limited to smaller objects so that the quantitative phase values are correct for each object. Using a 100 μm condenser pinhole will allow us to greatly reduce the halo effect in images from most biological samples while still maintaining a good SNR. The shortest exposure time obtained using a 100 μm pinhole in the condenser and a 10 μm physical pinhole in the SLM plane was 360 ms. The typical exposure time for wDPM with NA_{con} = 0.09 is about 10-20 ms.

In order to capture faster dynamics and/or to measure larger objects without introducing artifacts, we need to increase source brightness. This can be accomplished using a supercontinuum laser (SCL). Figure 8(a) shows the spectrum of YSL's SC-1.5-HE model, 1.5W blue enhanced SCL. The infrared (IR) portion of the spectrum was blocked using a shortpass filter (Thorlabs FESH0750) with a cut-off wavelength of 750 nm. Figure 8(b) show the 0th order reference amplitude image illustrating the uniformity. Figures 8(c)-8(f) show the recovered height maps and corresponding cross-sections of square micropillars of various lateral dimensions. The measured heights are correct and the images are free of halo and shade-off artifacts. This is due to the fact that, while the SCL is temporally broadband (white light), it has adequate spatial coherence without any additional filtering by the condenser aperture. Furthermore, the SCL source can deliver a much brighter illumination field for a given spatial coherence area yielding superior SNR and allowing for significantly faster dynamic measurements, including those of structures that have arbitrary lateral size, without

introducing artifacts. For example, the exposure time can be set to the camera's minimum, which is 400 μs. Note however that in Fig. 8, the exposure time was set to 10 ms and a neutral density filter attenuated the SCL power so that a fairer comparison could be made between the SCL data and the halogen data in Figs. 4 and 5 with $NA_{con} = 0.09$.
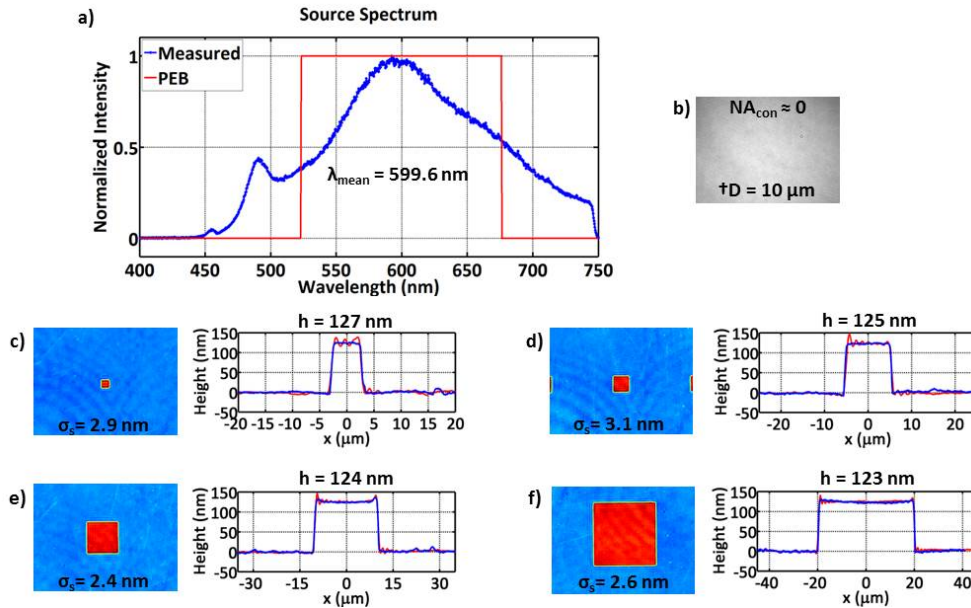

Fig. 8. DPM using an SCL with a 750nm shortpass filter. (a) Spectrum of the SCL source with power-equivalent bandwidth (PEB) approximation. The mean wavelength is 599.6 nm. (b) 0th order reference amplitude image is uniform. (c-f) Recovered height images and corresponding cross-sections for 5, 10, 20, and 40 μm wide square pillars, respectively. The cross-section figure shows wDPM profile in red and the Alpha Step profile in blue. † denotes a physical pinhole in the SLM plane.

4. Conclusions

We have demonstrated that object-dependent artifacts such as halo and shade-off in white light DPM can be caused by a lack of spatial coherence, which prevents the lower spatial frequencies of the structure from being recovered correctly. Obtaining adequate spatial coherence at the condenser aperture as well as performing proper spatial filtering in the SLM plane are both necessary to recover quantitatively correct height maps. A clear reduction in the halo and negative dimple of red blood cells was demonstrated by computing the required condenser pinhole size in order to achieve adequate spatial coherence for the given specimen. We also demonstrated that a supercontinuum laser can be used to obtain accurate topographical measurements with minimal exposure times.

Appendix

A1. Temporal coherence

In this section, we assess the temporal coherence and show that it is not an issue under our typical imaging conditions. To quantify the temporal coherence, the source spectrum was measured and used to compute the temporal autocorrelation function. The temporal coherence length was then extracted. Figure 9(a) shows the source spectrum taken from the wDPM system (HAL 100 Halogen Lamp, Z2 Axio-Imager, Zeiss) at T = 3200 K, where T is the color temperature of the halogen lamp.

The spectrum was measured using a standard spectrometer (Ocean Optics Spectrometer USB 2000+). Several spectra were taken in different planes including the sample plane,

camera plane, and directly off the source. All of these measurements resulted in the same center wavelength and temporal coherence value.

The autocorrelation function was then calculated using MATLAB and the temporal coherence was extracted by looking at the distance along the optical axis where the envelope was greater than half its maximum value. Figure 9(b) shows the autocorrelation function of the source along with its envelope computed via a Hilbert transform. The measured temporal coherence length using this approach was 2.1 μm. The temporal coherence length of white light systems is typically on the order of a couple of microns depending on both the source spectrum and the definition of coherence length used in the calculation [31].
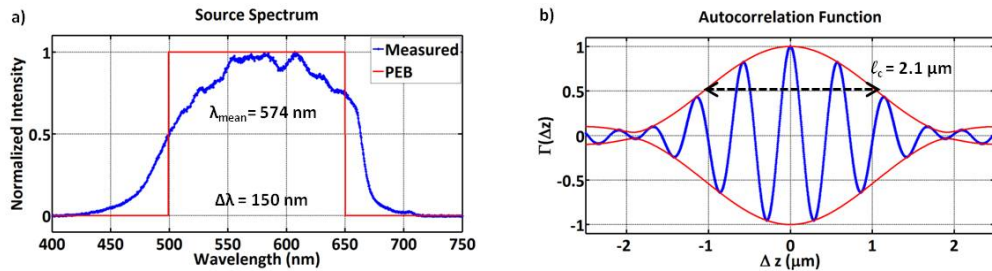

Fig. 9. Temporal coherence of the wDPM imaging system. (a) Spectrum of the HAL 100 halogen lamp showing the power-equivalent bandwidth (PEB) approximation. The center wavelength at a color temperature of 3200 K is 574 nm. This wavelength is used to convert the measured phase to height. (b) Temporal autocorrelation function and its envelope obtained via a Hilbert transform. The temporal coherence length obtained from the envelope is 2.1 μm.

The temporal coherence length indicates the maximum optical path length (OPL) difference over which we can obtain interference and thus accurately measure height. Most biological specimens in their typical imaging media exhibit low index contrast. For example, red blood cells (RBCs) in Coulter solution have a very low index contrast of $\Delta n \approx 0.06$ [32]. For a lower Δn, a larger height (i.e. h = 2.0 / 0.06 = 33 μm) can be measured for a given temporal coherence length. Thus, we can measure most biological specimens without any issues regarding the temporal coherence. Further, the maximum thickness we can measure without issues is 3.9 μm for quartz pillars in air and 27 μm for polystyrene beads in immersion oil. Thus, the source has an order of magnitude larger temporal coherence than what is needed to measure the samples in this paper.

It is also important to mention that phase unwrapping errors can occur when the measured phase jumps by more than 2π between adjacent pixels. For most biological structures, changes in height are gradual and this is not an issue. However, for semiconductor samples such as dry etched structures with vertical sidewalls, this may be a concern depending on the height. Both the temporal coherence and phase ambiguity should be considered before imaging a particular sample. Phase unwrapping errors can be eradicated by employing different wavelength lasers (i.e., 2 or more) or by using a color camera to separate the red-green-blue (RGB) planes under white light illumination [33–35].

Acknowledgments